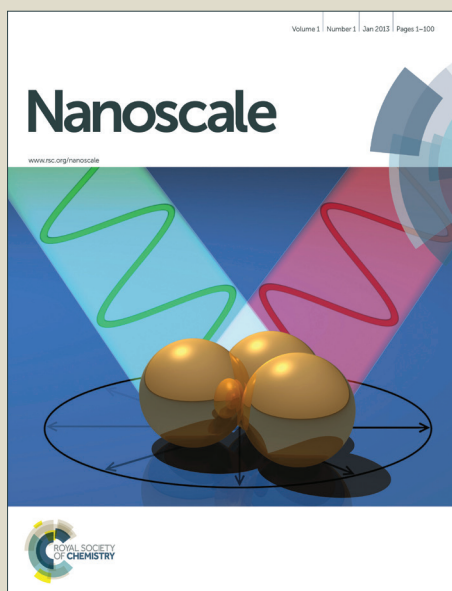


# Nanoscale

Accepted Manuscript



This is an *Accepted Manuscript*, which has been through the Royal Society of Chemistry peer review process and has been accepted for publication.

*Accepted Manuscripts* are published online shortly after acceptance, before technical editing, formatting and proof reading. Using this free service, authors can make their results available to the community, in citable form, before we publish the edited article. We will replace this *Accepted Manuscript* with the edited and formatted *Advance Article* as soon as it is available.

You can find more information about *Accepted Manuscripts* in the [Information for Authors](#).

Please note that technical editing may introduce minor changes to the text and/or graphics, which may alter content. The journal's standard [Terms & Conditions](#) and the [Ethical guidelines](#) still apply. In no event shall the Royal Society of Chemistry be held responsible for any errors or omissions in this *Accepted Manuscript* or any consequences arising from the use of any information it contains.

## ARTICLE

# Nanoscale voxel spectroscopy by simultaneous EELS and EDS tomography

Cite this: DOI: 10.1039/x0xx00000x

Georg Haberfehlner,<sup>a</sup> Angelina Orthacker,<sup>a</sup> Mihaela Albu<sup>a</sup>, Jiehua Li<sup>b</sup> and Gerald Kothleitner<sup>a,c</sup>

Received 00th January 2012,

Accepted 00th January 2012

DOI: 10.1039/x0xx00000x

[www.rsc.org/](http://www.rsc.org/)

Extending the capabilities of electron tomography with advanced imaging techniques and novel data processing methods, can augment the information content in three-dimensional (3D) reconstructions from projections taken in the transmission electron microscope (TEM). In this work we present the application of simultaneous electron energy-loss spectroscopy (EELS) and energy-dispersive X-ray spectroscopy (EDS) to scanning TEM tomography. Various tools, including refined tilt alignment procedures, multivariate statistical analysis and total-variation minimization enable the 3D reconstruction of analytical tomograms, providing 3D analytical metrics of materials science samples at the nanometer scale. This includes volumetric elemental maps, and reconstructions of EDS, low-loss and core-loss EELS spectra as four-dimensional spectrum volumes containing 3D local voxel spectra. From these spectra, compositional, 3D localized elemental analysis becomes possible opening the pathway to 3D nanoscale elemental quantification.

## Introduction

Electron tomography extends the imaging capabilities of a transmission electron microscope (TEM) to the third spatial dimension.<sup>1</sup> Several contrast mechanisms in the TEM have been successfully used in tomography to access a wide range of information at the nanoscale in three dimensions (3D).<sup>2–5</sup> In materials science, especially high-angle annular dark-field (HAADF) imaging in the scanning transmission electron microscope (STEM) has proven to be a powerful tool due to its atomic number sensitivity and robustness to diffraction contrast.<sup>6–11</sup>

Analytical electron microscopy, based on inelastic electron scattering, generates spectroscopic and element-sensitive imaging data. Its combination with electron tomography can allow chemically sensitive 3D imaging with nanometer (or even atomic) resolution. Initially energy-filtered TEM (EFTEM) tomography<sup>2,12–17</sup> and more recently energy-dispersive X-ray spectroscopy (EDS)<sup>18–20</sup> and electron energy-loss spectroscopy (EELS)<sup>21,22</sup> tomography in the STEM have been demonstrated. This has resulted in the possibility to reconstruct elemental distributions in 3D. The first reconstructions of spectral information have been demonstrated in the low-loss regime using EFTEM<sup>13,15</sup> for few spectral channels and more recently also using EELS for identification of surface plasmons.<sup>5</sup> Very recently also reconstruction of core-loss EELS spectra has been demonstrated by reconstructing few independent spectral components.<sup>23</sup> However, the quality of such reconstructions was often constrained by limited tilt ranges, small number of pixels, lengthy acquisition times or a lack of full spectroscopic X-ray and energy-loss data. For the same reasons, as well as due the computational complexity involved, simultaneous EELS and EDX tomography including full synthesis of 3D

local X-ray and energy-loss spectra based on an independent reconstruction of each spectral channel has not yet been demonstrated.

In this work EELS and EDS tomographic data was acquired simultaneously and subsequently subject to advanced data processing methods to extract precise 3D elemental maps as well as EELS and EDS voxel spectra: A powerful projection/re-projection matching algorithm for reliable alignment of the tomographic data was applied,<sup>24</sup> as well as multivariate statistical analysis for noise reduction of EELS spectra.<sup>25,26</sup> Spectra have been evaluated with a new model-based approach,<sup>27,28</sup> and compressed sensing<sup>9,10,29–32</sup> was established for the 3D reconstruction of elemental maps. Though these techniques have been used separately in analytical microscopy or electron tomography, their combined application opens the route for an advanced analytical 3D investigation.

Two ways to examine analytical electron tomography data have been pursued in this work. These are outlined in Fig. 1. In a STEM, tilt angle resolved spectrum images were acquired, recording EDS, low-loss and core-loss EELS spectra simultaneously for each pixel. This results in four-dimensional (4D) datasets, where each dataset consists of two spatial, one energy and a fourth tilt angle dimension. In our first approach towards 3D chemical imaging, 2D elemental maps have been extracted for each tilt angle from the spectrum images (A1 in Fig. 1), giving tilt-dependent EELS and EDS chemical information for every element under consideration. By tomographic reconstruction (A2 in Fig. 1) each tilt-dependent map was used to reconstruct a three-dimensional element-specific volume. In our second approach EELS and EDS spectra were directly reconstructed from the spectrum image tilt series by doing one reconstruction for each individual spectral channel (B in Fig. 1), yielding 4D datasets – spectrum volumes

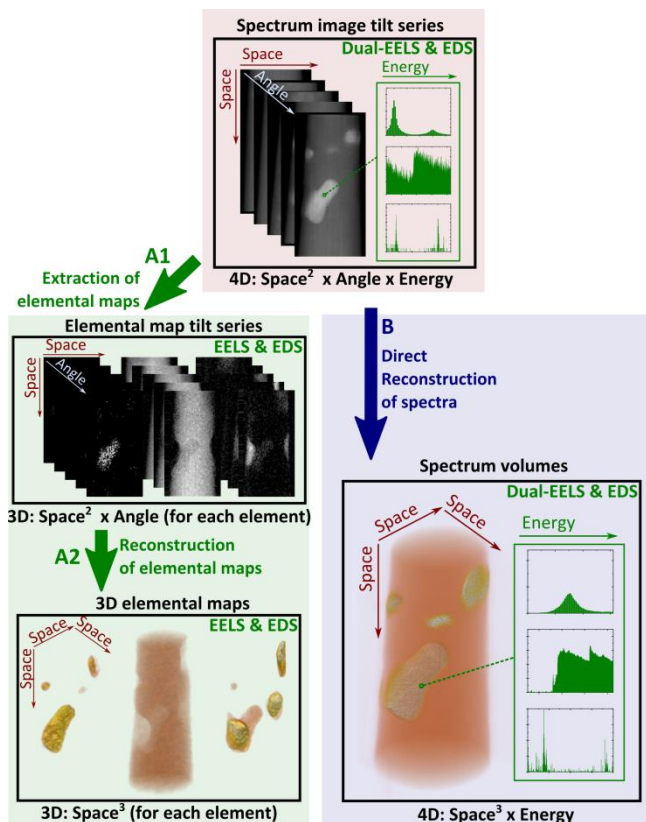


**Fig. 1** Principles of analytical electron tomography showing the two approaches (A&B) pursued in this work.

– that consist of three spatial and one energy dimension. 3D local voxel spectra could then be extracted and analyzed to access local chemical information on a spectral rather than an image basis.

## Results & Discussion

The procedures involved in analytical electron tomography are demonstrated on an Al-5 wt.% Si alloy with 50 ppm Na and 6100 ppm Yb. Modification and refinement of eutectic Si in Al-Si alloys by trace elements is a widely used method to improve mechanical properties of casting alloys.<sup>33–37</sup> Nevertheless the modification and refinement mechanisms are still a matter of debate and require understanding of the elemental distribution down to the atomic level.<sup>35</sup> A needle shaped sample, suitable for tomography, was prepared from the surface of the Al-Si sample using focused ion beam (FIB) milling<sup>38,39</sup> (see Supplementary Information).

Analytical electron tomography experiments were performed on a probe-corrected FEI Titan<sup>3</sup> G2 60–300 microscope with an X-FEG Schottky field-emission electron source operated at 300 kV (see Supplementary Information for details). The microscope is equipped with a Gatan Imaging Filter (GIF) Quantum<sup>40</sup> and a FEI Super-X EDS detector, consisting of four separate silicon drift detectors.<sup>41</sup> The microscope setup allows fast parallel acquisition of EDS data as well as of low-loss and core-loss EELS spectra using the dual-EELS capacity of the GIF Quantum.<sup>42–44</sup> Thanks to this experimental setup spectrum images of about 100\*200 pixels with a pixel size of 1 nm could be acquired every 5° over a tilt range from -75° to +80°. Fig. 2 shows HAADF STEM images acquired at different tilt angles

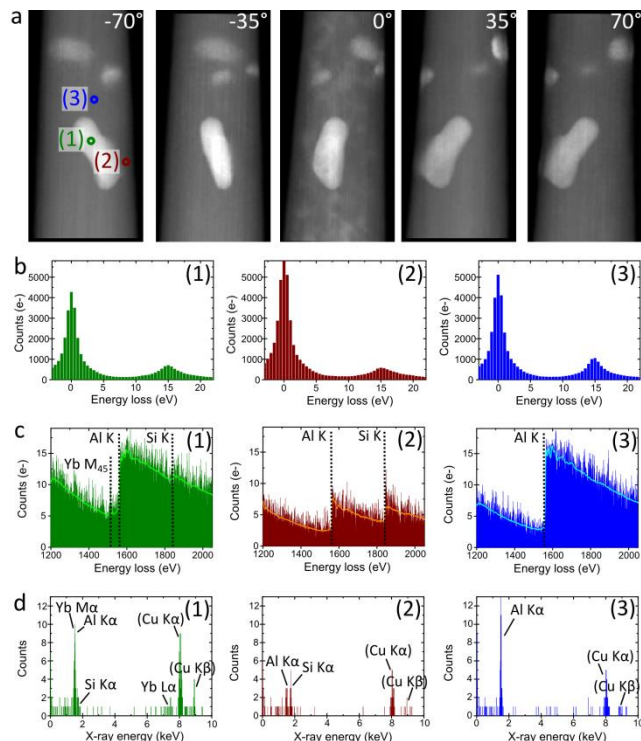


**Fig. 2** (a) HAADF STEM images from tilt series. (b) Single pixel low-loss EELS spectra. (c) Single pixel core-loss EELS spectra (original spectra are shown as histogram, PCA-treated spectra as solid lines) (d) Single pixel EDS spectra. Spectra are taken from the locations indicated by (1), (2) and (3) in (a). In (c)&(d) ionization edges and X-ray absorption lines are indicated. Spurious signals from the microscope and sample holder (Cu) are shown in brackets. The Cu signal is strong at high tilt angles (-70°) as a part of the scattered electrons hit the sample support.

and EDS and EELS spectra from single pixels in the projections.

The tilt series alignment was carried out via HAADF STEM images, acquired together with the analytical data. The alignment process, which requires all projections to be registered to a common tilt axis located in the center of the projections, was a two-stage process. We started with an initial coarse alignment using filtered cross-correlation between neighboring images for first estimates of the shift parameters. These shift parameters were then refined in several iterations using projection/re-projection matching. Similar methods have been described previously and have shown to provide a reliable alignment.<sup>24,45</sup> In our workflow, a temporary reconstruction with the current alignment parameters is calculated, which is then re-projected at the orientations of the acquired projections. The shift between these re-projections and the acquired projections is determined using filtered cross-correlation with sub-pixel accuracy.<sup>46</sup> To calculate the position of the tilt axis, rotational centers were calculated for each sinogram by center of mass methods.<sup>47</sup> The shift and rotational alignments were done alternately, cycling through 10 iterations. This provided a set of alignment parameters, which was subsequently applied to all acquired analytical data.

A further challenge in the reconstruction arises from the low signal-to-noise ratio in core-loss EELS data, for edges beyond 1000 eV as for the material investigated (Yb-M<sub>45</sub>: 1528 eV, Al-

K: 1560 eV, Si-K: 1839 eV). The short pixel times in addition to low ionization cross-sections render the spectral processing with respect to background removal or thickness deconvolution problematic. Furthermore, the Yb-M<sub>45</sub> edge is overlapping with the Al-K edge, which complicates a separation of the net signal of those two edges.

Principal components analysis (PCA) has been shown to be able to overcome noise problems in EELS spectra.<sup>22,25,26</sup> We apply weighted PCA,<sup>26</sup> adapted to the dominant Poissonian noise in our EELS spectra (see Supplementary Information including Figure S1). Examples for such spectra are shown in Fig. 2b(2) superimposed with the original data. Noise reduction using PCA was necessary for further processing of spectral data. In untreated spectra the noise was too high to allow reliable extraction of the background and element specific signals in particular concerning separation of contributions from Yb and Al. For extraction of elemental maps from EELS spectrum images a model-based fitting approach was used.<sup>28</sup> The spectrum is modelled using a background, described with a power-law function and ionization edges, given by Hartree-Slater cross-sections. Plural scattering can be included in the model by convolution of the single-scattering core-loss model with the low-loss spectrum. Furthermore the low-loss spectrum was used for modelling the electron-loss near-edge structure (ELNES) by an iterative refinement of ELNES intensities. To extract elemental maps from projections, PCA-treated core-loss spectra and the corresponding low-loss spectra were used (see Supplementary Information including Figure S2). The extracted EELS elemental maps correspond to the extracted signal

normalized by the elemental cross-sections.

For extraction of EDS maps also a model-based approach was used, describing the background with a Kramers-model.<sup>48</sup> After identification of the X-ray lines, Gaussian peaks were fitted for each line family and the integral from the whole series was used to generate the element-specific signal. The fitting approach is useful in particular for extraction of Al-elemental maps as the Al K-lines (Al-K $\alpha$ : 1.49 keV) are very close to the Yb M-lines (Yb-M $\alpha$ : 1.52 keV). For Si the K-lines (Si-K $\alpha$ : 1.74 keV) and for Yb the L-lines (Yb-L $\alpha$ : 7.41 keV) were used. The extracted EDS elemental maps correspond to the sum of X-ray counts for a specific element. In our setup, the extracted intensity of the elemental maps displayed a strong angular dependence due to shadowing of X-rays by the sample holder. This was compensated by normalizing the projections with the summed intensity from each elemental map at the respective tilt. This was possible since effects of X-ray absorption in the sample could be neglected due to the small sample size (see Supplementary Information including Figure S3 and Table S1). The 3D elemental maps were reconstructed with a total variation (TV) minimization algorithm. For comparison reconstructions with the simultaneous iterative reconstruction technique (SIRT) were also carried out. TV minimization denotes a variant of compressed sensing.<sup>49,50</sup> It is assumed that the image (or volume) gradient is sparse, i.e. is zero at most locations. Because of the materials chemistry and the sharp interfaces between the different phases in the sample, the assumption was justified. For TV minimization the problem was solved.<sup>51</sup> In this formulation the first term is the isotropic

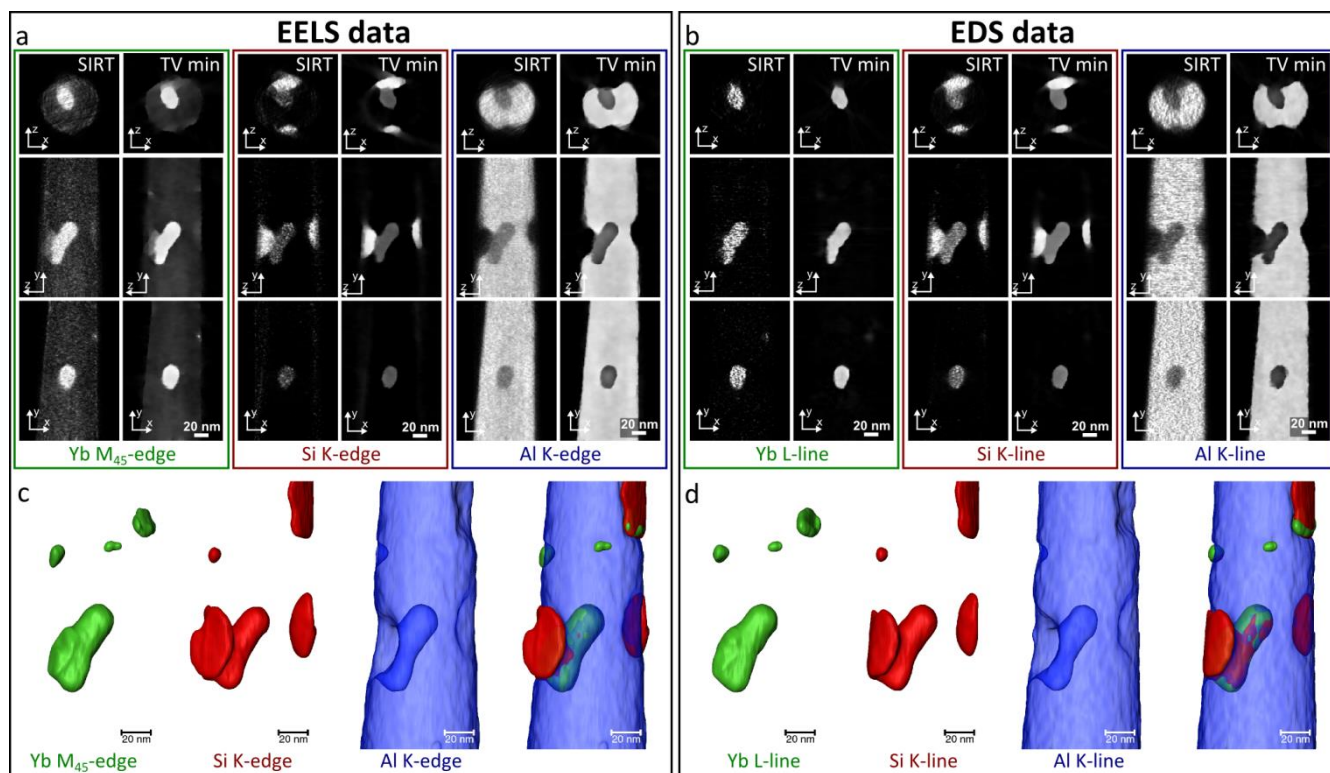


**Fig. 3** (a) Orthogonal slices through reconstructions of the Yb M<sub>45</sub>-edge, the Si K-edge and the Al K-edge from EELS data. (b) Orthogonal slices through reconstructions of the Yb L-line, the Si K-line and the Al K-line from EDS data. (c) Surface rendered views of the segmented volume of the Yb M<sub>45</sub>-edge, the Si K-edge and the Al K-edge and an overlay of the three segmented volumes. (d) Surface rendered views of the segmented volume of the Yb L-line, the Si K-line and the Al K-line and an overlay of the three segmented volumes.

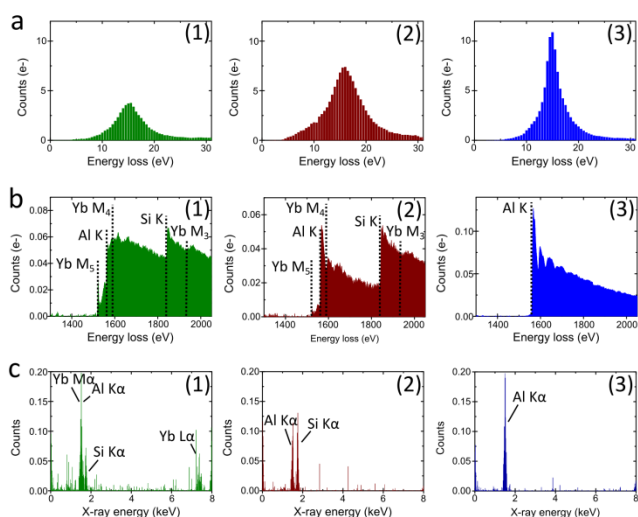


**Fig. 4** Reconstructed single voxel spectra (voxel size:  $1 \text{ nm}^3$ ). (a) Single-scattering low-loss EELS spectra, (b) single-scattering core-loss EELS spectra (PCA treated) and (c) EDS spectra. Ionization edges and major X-ray lines are indicated. Spectra are extracted (1) from an Yb-rich precipitate, (2) from a Si-rich region, (3) from Al.

$$\min_{u \in \mathbb{R}^{3n}} \sum_i \|D_i u\|_2 + \frac{\mu}{2} \|Au - b\|_2^2 \quad (1)$$

TV norm of the image or volume vector  $u$ .  $D_i u$  is the local gradient vector at the position  $i$  in three dimensions. This 3D implementation of the algorithm provides more reliable reconstructions compared to previous implementations of TV minimization where the gradient  $D_i U$  was usually calculated along 2 dimensions<sup>29–32</sup>. The second term in (1) represents a least-squares optimization of the linear equation system given by the projection geometry.  $b$  is the measurement vector containing all projection data.  $A$  is the projection operator mapping from the image or volume vector  $u$  to a projection vector.<sup>52</sup>  $\mu$  is a weighting factor between the two terms in the optimization and needs to be adapted to the noise level in the projections. (see Supplementary Information including Fig. S4 for a comparison of reconstructions using 2D and 3D algorithms and different weighting factors  $\mu$ )

Slices through 3D EELS elemental maps of the major constituents of the sample are displayed in Fig. 3a for both SIRT and TV minimization. The same slices through 3D EDS elemental maps are depicted in Fig 3b. TV minimization provided sharp interfaces in the reconstruction and allowed simple segmentation of the reconstruction based on absolute threshold values using the Otsu threshold criterion.<sup>53</sup> Fig. 3c&d and Supplementary Videos S1&S2 show surface rendered views of segmented 3D EELS and EDS elemental maps respectively.

TV minimization applied to the reconstruction of elemental maps was very efficient regarding noise reduction. In the case of silicon, it is easily possible to distinguish regions with a higher Si-concentration from regions with a lower Si-concentration, where also Yb is present. Good agreement can be observed between the reconstructions from EELS and EDS data.

To extract more information about local material compositions we reconstructed 3D local EDS and EELS spectra for each voxel (cf. approach B in Fig. 1). For EELS plural scattering was removed,<sup>54</sup> so single-scattering spectra could be reconstructed.

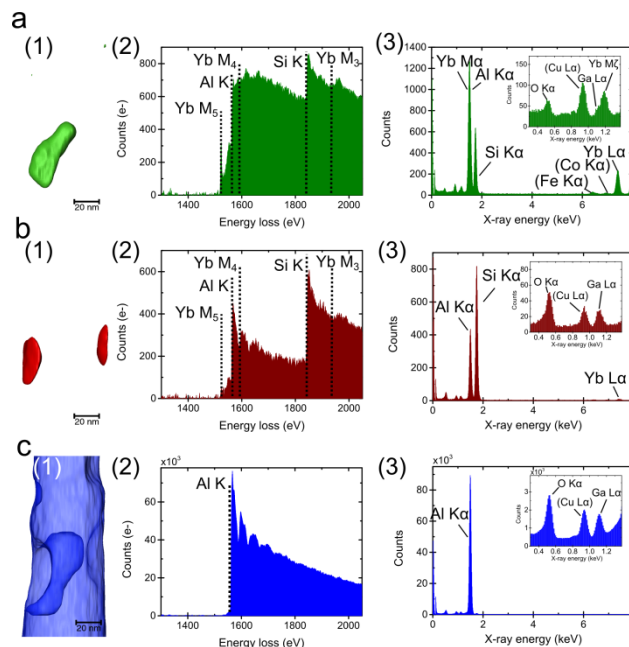


**Fig. 5** Local core-loss EELS and EDS spectra summed over different regions of the volume: (a) summed over Yb-rich precipitates, (b) summed over Si-rich regions, (c) summed over the Al-matrix without the surface layer. (1) shows the masks over which spectra are summed, (2) shows the core-loss EELS spectra, (3) shows EDS spectra, the inset in (3) shows a zoom to the low-energy region from 0.5 keV to 1.3 keV. Ionization edges and X-ray lines are indicated. Absorption lines arising due to the instrument and sample support (Cu, Fe, Co) are written in brackets. Ga and O are present due to Ga-ion implantation during sample preparation and surface oxidation.

Depending on the energy regime either Fourier-log (low-loss) or Fourier-ratio (high-loss) deconvolution was carried out. EELS core-loss spectra had been PCA treated beforehand. For the reconstruction each spectral channel was treated as an independent tilt series and was reconstructed using a multiplicative SIRT algorithm with 30 iterations (see Supplementary Information). This process resulted in physically meaningful reconstructions, as every voxel spectrum represents the local single scattering probability. In the EDS case, again spectra normalized to compensate shadowing effects were reconstructed (see Supplementary Information). Since X-ray intensities are proportional to the probability of X-ray creation along the beam path through the sample, the reconstructed voxel spectra contain information about the 3D local X-ray creation probability. Fig. 4 shows single-voxel spectra (voxel size:  $1 \text{ nm}^3$ ) from different locations in the sample. Different absorption edges and X-ray lines as well as changes in their relative intensity can be clearly distinguished. Being able to reconstruct the 3D elemental maps and local voxel spectra allows combining the information from both. Using all reconstructed data we sum 3D voxel spectra over specific regions defined by masks created from the 3D EDS elemental maps. To reduce the impact of interfaces between the different materials, the boundaries of the masks were removed by applying 3D morphological erosion operators. These 3D masks and EDS and EELS voxel spectra summed over the different regions are shown in Fig. 5. This provides spectra with

high signal to noise ratio but which contain only information about a single phase in three dimensions. Such matrix-free spectra cannot be analyzed from 2D spectrum images as spectra of localized phases are also affected by other materials over the thickness of the sample.

With voxel spectra being available, relative phase compositions could be derived, harnessing the strengths of the respective EELS and EDS quantification schemes, yet encountering some typical issues, associated with overlapping signals or inaccurate sensitivity factors. Quantification of the Yb-rich precipitates (Fig. 5a) gave Al:Si:Yb compositions of at.% 43:47:10 in EELS and at.% 48:35:16 for EDS (see Supplementary Information). In the present case the main limitation are overlapping Yb-M and Al-K edges and X-ray lines. Furthermore for the EELS case the  $M_{45}$ -edge of Yb is not well modelled by the Hartree-Slater cross-section model. EDS quantification is based on k-factors, which are not known with high accuracy. Despite the observed compositional variation between the techniques, these values give a fair estimate about the relative composition. This also shows the usefulness of simultaneous EELS and EDS analysis, as the complementarity of the two techniques serves to validate results from one technique by the other.

## Conclusions

In the present work simultaneous analytical EELS and EDS tomography for 3D nanoscale chemically sensitive microscopy was established. While conventional tomographic techniques, such as HAADF STEM tomography, can only provide indications about chemistry, 3D elemental maps can provide unambiguous elemental identification and reveal compositional changes. Elemental identification removes many uncertainties in the interpretation of tomograms. We demonstrated the feasibility of reconstructing spectrum volumes for both EELS and EDS reconstructing each spectral channel individually. These four-dimensional datasets contain local voxel spectra, which allow the local access of different regions in the sample. In this way a 3D matrix-free analysis of confined phases, such as nanoparticles or precipitates, becomes possible. This is an important step towards reliable compositional quantification in 3D space. We have shown that data processing methods, such as projection/re-projection matching, multivariate statistical analysis and compressed sensing, can enable reliable reconstructions of analytical tomograms, even from data limited in terms of pixel time, number of pixels and the number of spectrum images.

Simultaneous EELS and EDS tomography allows verification of one technique by the other, but it will also be useful when some elements in a sample are easier to detect by one technique or the other. Furthermore linking analytical tomography with complementary techniques, such as atom probe tomography<sup>55</sup> will allow a deeper understanding of materials and techniques. Apart from elemental quantification EELS tomography has the potential for extraction of local electrical and optical properties or chemical fingerprinting in three dimensions. The low-loss spectrum contains a large amount of information about material properties, in the core-loss spectrum ELNES analysis can provide information about the chemical state in 3D. These methods will be applicable to a wide range of materials, essentially to all applications where 3D nanometer resolution is required in combination with chemical sensitivity. Examples are all types of embedded nanoparticles, core/shell structures, precipitation studies or the investigation of dopants.

Another interesting goal of analytical electron tomography – next to reliable quantification – will be to combine chemical sensitivity with 3D atomic resolution. The main challenges lie in the long acquisition times compared to HAADF STEM, where atomic resolution tomography has already been demonstrated. Spectrum images with high enough signal to noise ratio need to be recorded, while limiting beam damage and sample drift during image acquisition.

## Acknowledgements

This research has received funding from the European Union within the 7<sup>th</sup> Framework Program [FP7/2007-2013] under Grant Agreement no. 312483 (ESTEEM2) and from the Austrian Forschungsförderungsgesellschaft (FFG) in the OPTIMATSTRUCT project. We thank Evelin Fisslthaler, Johanna Kraxner and Werner Grogger from FELMI-ZFE Graz and Peter Schumacher from Chair of Casting Research, University of Leoben for discussions and advise as well as Paul Thomas, Ray Twesten and Bernd Kraus from Gatan for providing software prototypes for EELS and EDS analysis. Open-source software code has been used: The TV minimization solver TVAL3 (<http://www.caam.rice.edu/~optimization/L1/TVAL3/>), the tomographic reconstruction toolbox ASTRA (<http://sourceforge.net/projects/astra-toolbox/>) and the spectral data analysis toolkit Hyperspy (<http://hyperspy.org/>).

## Notes and references

<sup>a</sup> Graz Centre for Electron Microscopy, Steyrergasse 17, 8010 Graz, Austria.

<sup>b</sup> Chair of Casting Research, Department of Metallurgy, University of Leoben, Franz-Josef-Strasse 18, 8700 Leoben, Austria.

<sup>c</sup> Institute for Electron Microscopy and Nanoanalysis, Graz University of Technology, Steyrergasse 17, 8010 Graz, Austria.

† Electronic Supplementary Information (ESI) available: Electron tomography videos, methods including sample preparation, image acquisition and data processing, estimation of X-ray absorption, and comparison of reconstruction parameters. See DOI: 10.1039/b000000x/

1. P. A. Midgley and R. E. Dunin-Borkowski, *Nat. Mater.*, 2009, **8**, 271–280.
2. G. Möbus, R. C. Doole, and B. J. Inkson, *Ultramicroscopy*, 2003, **96**, 433–451.
3. A. J. Koster, R. Grimm, D. Typke, R. Hegerl, A. Stoschek, J. Walz, and W. Baumeister, *J. Struct. Biol.*, 1997, **120**, 276–308.
4. J. S. Barnard, J. Sharp, J. R. Tong, and P. A. Midgley, *Science*, 2006, **313**, 319.
5. O. Nicoletti, F. de la Peña, R. K. Leary, D. J. Holland, C. Ducati, and P. A. Midgley, *Nature*, 2013, **502**, 80–84.
6. P. A. Midgley and M. Weyland, *Ultramicroscopy*, 2003, **96**, 413–431.
7. S. Van Aert, K. J. Batenburg, M. D. Rossell, R. Ermi, and G. Van Tendeloo, *Nature*, 2011, **470**, 374–377.
8. M. C. Scott, C.-C. Chen, M. Mecklenburg, C. Zhu, R. Xu, P. Ercius, U. Dahmen, B. C. Regan, and J. Miao, *Nature*, 2012, **483**, 444–447.
9. B. Goris, S. Bals, W. Van den Broek, E. Carbó-Argibay, S. Gómez-Graña, L. M. Liz-Marzán, and G. Van Tendeloo, *Nat. Mater.*, 2012, **11**, 930–935.
10. B. Goris, A. De Backer, S. Van Aert, S. Gómez-Graña, L. M. Liz-

- Marzán, G. Van Tendeloo, and S. Bals, *Nano Lett.*, 2013, **13**, 4236–4241.
11. C.-C. Chen, C. Zhu, E. R. White, C.-Y. Chiu, M. C. Scott, B. C. Regan, L. D. Marks, Y. Huang, and J. Miao, *Nature*, 2013, **496**, 74–77.
12. G. Möbus and B. J. Inkson, *Appl. Phys. Lett.*, 2001, **79**, 1369–1371.
13. M. H. Gass, K. K. K. Koziol, A. H. Windle, and P. A. Midgley, *Nano Lett.*, 2006, **6**, 376–379.
14. I. Florea, O. Ersen, C. Hirlimann, L. Roiban, A. Deneuve, M. Houille, I. Janowska, P. Nguyen, C. Pham, and C. Pham-Huu, *Nanoscale*, 2010, **2**, 2668–2678.
15. G. Haberfehlner, P. Bayle-Guillemaud, G. Audoit, D. Lafond, P. H. Morel, V. Jousseume, T. Ernst, and P. Bleuet, *Appl. Phys. Lett.*, 2012, **101**, 063108.
16. M. Weyland and P. A. Midgley, *Microsc. Microanal.*, 2003, **9**, 542–555.
17. R. D. Leapman, E. Kocsis, G. Zhang, T. L. Talbot, and P. Laquerriere, *Ultramicroscopy*, 2004, **100**, 115–125.
18. Z. Saghi, X. Xu, Y. Peng, B. Inkson, and G. Möbus, *Appl. Phys. Lett.*, 2007, **91**, 251906.
19. K. Lepinay, F. Lorut, R. Pantel, and T. Epicier, *Micron*, 2013, **47**, 43–49.
20. A. Genc, L. Kovarik, M. Gu, H. Cheng, P. Plachinda, L. Pullan, B. Freitag, and C. Wang, *Ultramicroscopy*, 2013, **131**, 24–32.
21. K. Jarausch, P. Thomas, D. N. Leonard, R. Twesten, and C. R. Booth, *Ultramicroscopy*, 2009, **109**, 326–337.
22. L. Yedra, A. Eljarrat, R. Arenal, E. Pellicer, M. Cabo, A. López-Ortega, M. Estrader, J. Sort, M. D. Baróe, S. Estradé, and F. Peiró, *Ultramicroscopy*, 2012, **122**, 12–18.
23. L. Yedra, A. Eljarrat, J. M. Rebled, L. López-Conesa, N. Dix, F. Sánchez, S. Estradé, and F. Peiró, *Nanoscale*, 2014, **6**, 6646–6650.
24. T. Uusimäki, G. Margarit, K. Trohidou, P. Granitzer, K. Rumpf, M. Sezen, and G. Kothleitner, *Nanoscale*, 2013, **5**, 11944–11953.
25. M. Bosman, M. Watanabe, D. T. L. Alexander, and V. J. Keast, *Ultramicroscopy*, 2006, **106**, 1024–1032.
26. F. de la Peña, M.-H. Berger, J.-F. Hochepeid, F. Dynys, O. Stephan, and M. Walls, *Ultramicroscopy*, 2011, **111**, 169–176.
27. J. Verbeeck and S. Van Aert, *Ultramicroscopy*, 2004, **101**, 207–224.
28. P. J. Thomas and R. D. Twesten, *Microsc. Microanal.*, 2012, **18**, 968–969.
29. Z. Saghi, D. J. Holland, R. Leary, A. Falqui, G. Bertoni, A. J. Sederman, L. F. Gladden, and P. A. Midgley, *Nano Lett.*, 2011, **11**, 4666–4673.
30. B. Goris, W. Van den Broek, K. J. Batenburg, H. Heidari Mezerji, and S. Bals, *Ultramicroscopy*, 2012, **113**, 120–130.
31. R. Leary, Z. Saghi, P. A. Midgley, and D. J. Holland, *Ultramicroscopy*, 2013, **131**, 70–91.
32. B. Goris, M. A. Van Huis, S. Bals, H. W. Zandbergen, L. Manna, and G. Van Tendeloo, *Small*, 2012, **8**, 937–942.
33. J. H. Li, M. Z. Zarif, G. Dehm, and P. Schumacher, *Philos. Mag.*, 2012, **92**, 3789–3805.
34. S. Haro-Rodríguez, R. E. Goytia-Reyes, D. K. Dwivedi, V. H. Baltazar-Hernández, H. Flores-Zúñiga, and M. J. Pérez-López, *Mater. Des.*, 2011, **32**, 1865–1871.
35. J. H. Li, M. Z. Zarif, M. Albu, B. J. McKay, F. Hofer, and P. Schumacher, *Acta Mater.*, 2014, **72**, 80–98.
36. K. Nogita, H. Yasuda, K. Yoshida, K. Uesugi, A. Takeuchi, Y. Suzuki, and A. K. Dahle, *Scr. Mater.*, 2006, **55**, 787–790.
37. K. Nogita, H. Yasuda, M. Yoshiya, S. D. McDonald, K. Uesugi, A. Takeuchi, and Y. Suzuki, *J. Alloys Compd.*, 2010, **489**, 415–420.
38. N. Kawase, M. Kato, H. Nishioka, and H. Jinnai, *Ultramicroscopy*, 2007, **107**, 8–15.
39. P. Bleuet, G. Audoit, J.-P. Barnes, J. Bertheau, Y. Dabin, H. Dansas, J.-M. Fabbri, B. Florin, P. Gergaud, A. Grenier, G. Haberfehlner, E. Lay, J. Laurencin, R. Serra, and J. Villanova, *Microsc. Microanal.*, 2013, **19**, 726–739.
40. A. Gubbens, M. Barfels, C. Trevor, R. Twesten, P. Mooney, P. Thomas, N. Menon, B. Kraus, C. Mao, and B. McGinn, *Ultramicroscopy*, 2010, **110**, 962–970.
41. P. Schlossmacher, D. O. Klenov, B. Freitag, and H. S. von Harrach, *Microsc. Today*, 2010, **18**, 14–20.
42. P. Longo and R. D. Twesten, *Microsc. Today*, 2013, **21**, 28–33.
43. G. Kothleitner, M. J. Neish, N. R. Lugg, S. D. Findlay, W. Grogger, F. Hofer, and L. J. Allen, *Phys. Rev. Lett.*, 2014, **112**, 085501.
44. G. Kothleitner, W. Grogger, M. Dienstleder, and F. Hofer, *Microsc. Microanal.*, 2014, **20**, 678–686.
45. H. Winkler and K. A. Taylor, *Ultramicroscopy*, 2006, **106**, 240–254.
46. M. Guizar-Sicairos, S. T. Thurman, and J. R. Fienup, *Opt. Lett.*, 2008, **33**, 156–158.
47. S. G. Azevedo, D. J. Schneberk, J. P. Fitch, and H. E. Martz, *IEEE Trans. Nucl. Sci.*, 1990, **37**, 1525–1540.
48. H. A. Kramers, *Philos. Mag.*, 1923, **46**, 836.
49. E. J. Candès, J. Romberg, and T. Tao, *IEEE Trans. Inf. Theory*, 2006, **52**, 489–509.
50. D. L. Donoho, *IEEE Trans. Inf. Theory*, 2006, **52**, 1289–1306.
51. C. Li, W. Yin, H. Jiang, and Y. Zhang, *Comput. Optim. Appl.*, 2013, **56**, 507–530.
52. W. J. Palenstijn, K. J. Batenburg, and J. Sijbers, *J. Struct. Biol.*, 2011, **176**, 250–253.
53. N. Otsu, *IEEE Trans. Syst. Man Cybern.*, 1979, **9**, 62–66.
54. R. F. Egerton, *Rep. Prog. Phys.*, 2009, **72**, 016502.
55. A. Grenier, S. Duguay, J. P. Barnes, R. Serra, G. Haberfehlner, D. Cooper, F. Bertin, S. Barraud, G. Audoit, L. Arnoldi, E. Cadet, A. Chabli, and F. Vurpillot, *Ultramicroscopy*, 2014, **136**, 185–192.